

A Systematic, Cross-Model Evaluation of Ensemble Light Scattering Sensors

Abhay Vidwans^{1,2}, Pratim Biswas^{1*}

¹Aerosol and Air Quality Research Laboratory, Department of Chemical, Environmental, and Materials Engineering, University of Miami, Coral Gables, FL 33146, USA

²Department of Energy, Environmental, and Chemical Engineering, Washington University in St. Louis, St. Louis, MO 63130, USA

ABSTRACT

The light scattering particulate matter sensor manufactured by Sharp Inc. (GP2Y1010AU0F) has been evaluated and compared to other commercial off-the-shelf sensors in previous studies and incorporated into commercial air quality monitors to measure aerosol concentration. Despite the popularity of this model, little attention has been given to the later models of the Sharp GP2Y sensor, whose optical chambers are identical but have modified circuitry with features such as enhanced sensitivity and precision. The signal processing front-end of the Sharp GP2Y was further modified by Texas Instruments in a robust analog front-end design with adjustable sensitivity. In this study, we examine six total sensors—the four currently available models of the Sharp GP2Y line dust sensors, and a sensor designed by the Texas Instruments set to two different sensitivity modes. Calibrations were performed in a simple aerosol chamber experiment, and correlations were performed to give rise to characteristic performance parameters of the sensor—sensitivity, precision, accuracy, saturation limit, and limit-of-detection. All six sensors had identical optics and geometry, isolating the effect of signal processing circuit topography on performance parameters for particulate matter measurement. Despite the identical optical chambers and components across the six light scattering sensors, all exhibited distinct performance parameters. Overall, the Sharp sensors performed consistently with the manufacturer claims; the GP2Y1023 exhibited the highest sensitivity ($3.16 \times 10^9 \text{ m}^2 \text{ W}^{-1}$ light sensitivity, $0.492 \text{ m}^3 \mu\text{g}^{-1}$ mass sensitivity) and the GP2Y1014 exhibited the highest precision ($\pm 10\%$ above $400 \mu\text{g m}^{-3}$). The Texas Instruments versions of the sensor exhibited significantly lower sensitivity ($< 0.1 \text{ m}^2 \text{ W}^{-1}$ light sensitivity and $< 0.03 \text{ m}^3 \mu\text{g}^{-1}$) than all Sharp GP2Y sensors, particularly when adjusted to low-gain mode. The low sensitivity of the Texas Instruments sensors makes them well-suited for high concentration environments. This study demonstrates how the performance of light scattering sensors can be readily quantified and how these parameters relate to the point-of-use.

OPEN ACCESS



Received: June 6, 2023

Revised: September 3, 2023

Accepted: November 6, 2023

* Corresponding Author:

pbiswas@miami.edu

Publisher:

Taiwan Association for Aerosol
Research

ISSN: 1680-8584 print

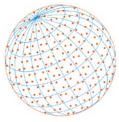
ISSN: 2071-1409 online

 **Copyright:** The Author(s). This is an open-access article distributed under the terms of the [Creative Commons Attribution License \(CC BY 4.0\)](https://creativecommons.org/licenses/by/4.0/), which permits unrestricted use, distribution, and reproduction in any medium, provided the original author and source are cited.

Keywords: Sensor, Light scattering, Low-cost sensor, COTS sensor, Particulate matter

1 INTRODUCTION

In recent years, low-cost particulate matter (PM) sensors have gained significant attention for improving the spatiotemporal resolution of PM concentration maps ([White et al., 2012](#); [Williams et al., 2014](#); [Kumar et al., 2015](#); [Lee et al., 2020](#)). Federal Reference Monitors are the EPA-approved state-of-the-art instruments that provide PM concentration based on cumulative measurement principles including particle inertia (cyclones, impactors), and real-time approaches such as gravimetry (TEOM) and interaction with beta radiation (BAMs) ([U.S. EPA, 2022](#)). While such monitors are robust and highly accurate, they are costly and sparsely distributed, leading to poor spatial resolution in PM data. The need for high-resolution PM maps has become particularly urgent in industrializing countries, where pollution is high and PM monitors are few ([Cao et al., 2013](#); [Gao et al., 2015](#); [Janssens-Maenhout et al., 2015](#)). Spatial resolution of PM data must be improved,



as uninformed inhabitants may be exposed to high concentrations of PM and suffer health consequences including heart and lung disease, and premature mortality (Pope *et al.*, 2002). Low-cost PM sensors can be utilized to capture the spatiotemporal variations in PM to keep citizens aptly informed of the air quality hazards in their region.

Low-cost sensors range from \$10 to a few \$100 (Li *et al.*, 2020) and operate by measuring light scattering. In brief, when a particle is illuminated, it scatters the light in all directions. The intensity of light scattered depends on particle-dependent parameters including its size, composition, and shape (Husar, 1974; Friedlander, 2000). A detector situated at a particular angle and distance relative to the light source will detect the scattered light. Instruments measuring light scattered by particles one-at-a-time are referred to as optical particle counters. Such instruments use a pump or fan to sample from ambient air, count particles, and output PM concentrations. While they are typically higher in cost, they can provide relatively accurate concentration measurements and, with adequate calibrations, provide particle size information (Manikonda *et al.*, 2016; Li *et al.*, 2020). Instruments measuring particles as a cloud are referred to as ensemble light scattering sensors. Ensemble scattering sensors are lower in cost due to their simplicity and compactness and have a faster response to environmental changes in PM due to their single-shot functionality. Some have been incorporated into commercial air quality monitors (Wang *et al.*, 2015; Manikonda *et al.*, 2016).

The Sharp GP2Y1010AU0F dust sensor is one of the most popular and well-researched ensemble light scattering sensors. It has been compared to other ensemble sensors and evaluated for performance (Wang *et al.*, 2015), calibrated rigorously against different aerosol sources (Li and Biswas, 2017), and evaluated in indoor PM exposure studies (Manikonda *et al.*, 2016) and occupational studies (Sousan *et al.*, 2016; Ghamari *et al.*, 2022). Since production of the 1010 model, Sharp Microelectronics has released several additional models in the dust sensor line, including a 1014, 1023, and 1026, boasting features including enhanced precision and sensitivity, temperature correction, and wider operating ranges. Texas Instruments developed an open-source analog front-end circuit board (TIDA-00378) (Martinez and Stout, 2015) to replace that of the Sharp sensors, using the same optical components and housing. Despite the availability and reported robustness of improved Sharp dust sensor models at a similar price point, recent studies continue to use the base model 1010 model, likely due to the momentum established from formative early studies. As a result, little attention has been given to the newer dust sensor models and no studies have validated manufacturer claims.

In this study, four models of the Sharp dust sensor (GP2Y1010AU0F, GP2Y1014AU0F, GP2Y1023AU0F, and GP2Y1026AU0F) and the Texas instruments analog front-end sensor (TIDA-00378) are systematically evaluated and compared for their sensitivity, precision, accuracy, limit-of-detection, and saturation limit. This study demonstrates a protocol for obtaining key performance parameters of light scattering sensors, and findings can validate the use of newer Sharp dust sensor models in low-cost PM studies. Further, we shed light on how the photodiode signal processing affects performance parameters of light scattering sensors, an area rarely touched upon in aerosol science literature.

2 METHODS

2.1 Sensor Models and Features

Table 1 summarizes the different Sharp-based sensor models evaluated in this study. The Sharp GP2Y1010AU0F (referred to “1010” for simplicity) is the base model. It is the most well-studied version and has been built into a commercial PM monitor (TSI AirAssure, UB Airsense). The 1014 model is nearly identical to the 1010 but features improved precision per its manual (Sharp, 2015b). While there are no technical details disclosed by the manufacturer, the block diagrams show three amplification circuits for the 1014 and only one for the 1010 (Sharp, 2020). Both sensors require external control for flashing the light source and output an analog signal that is directly related to scattered light. The newer versions, 1023 and 1026, have an internal microcomputer to control flashing of the light source (Sharp, 2015a, 2018). Both of these sensors output a digital signal. The 1023 outputs a pulsed signal; the width of this signal corresponds to

**Table 1.** Sensor specifications obtained from product spec sheets, and relevant studies.

Sensor Model	Features	Price	Commercial products	Studies	Output
GP2Y1010AU0F	Base model	\$12	TSI AirAssure UB AirSense	(Olivares <i>et al.</i> , 2012; Khadem and Sgârciu, 2014; Wang <i>et al.</i> , 2015; Li and Biswas, 2017; Vidwans <i>et al.</i> , 2022)	Analog
GP2Y1014AU0F	High precision	\$9	-	(Zhou <i>et al.</i> , 2020; Drogramaci and Butt, 2021; Baqer <i>et al.</i> , 2022)	Analog
GP2Y1023AU0F	High sensitivity Built-in IRED control Temperature correction	\$16	Sharp DN7C3CD015	(Kelleher <i>et al.</i> , 2018)	Digital, pulse width
GP2Y1026AU0F	High concentration Built-in IRED control Temperature correction	\$13	-	(Ghizlane <i>et al.</i> , 2022)	Digital, UART
TIDA-00378	Tunable signal gain Tunable IRED current	*	-	(Martinez and Stout, 2015)	Analog

* Full assembly not sold. Price varies based on cost of PCB fabrication and assembly.

the detected light. The 1026 outputs a digital UART (Universal Asynchronous Receiver/Transmitter) signal that can be transmitted to an external device. The 1023 and 1026 also contain a thermistor circuit which corrects the output based on temperature (Sharp, 2015a, 2018). There is very little detail provided on how this is done and why it is needed. In a previous study, it was shown that temperature has a minimal effect on the performance of the Sharp 1010 sensor (Wang *et al.*, 2015), hence temperature is not varied in this study. In contrast, the same study demonstrated that humidity affects the Sharp GP2Y1010 sensor output. We did not vary humidity in this study because no such correction mechanism is built into any Sharp sensor. The Texas Instruments version, TIDA-00378 (referred to as “TI sensor” for simplicity), features three potentiometers, two of which enable the user to fine-tune the signal gain. Its user manual (Martinez and Stout, 2015) elaborates on selection of resistors and capacitors to obtain the desired gain and frequency passband. A third potentiometer on the LED drive circuit allows the user to control current to the LED, effectively adjusting the incident light intensity of the particles. This potentiometer was set at its minimum value to maximize current to the IRED (Infrared Emitting Diode) to improve the signal-to-noise ratio. Two TI sensors were fabricated for this study. One was set to the highest gain value (lowest resistance values) and the other was set to the lowest gain value (highest resistance values) to study the effect of circuit parameters on performance of the sensors.

Fig. 1(a) shows the five sensors with the front shields removed. The 1010 and 1014 appear to be identical, but with different integrating circuits. The 1023, 1026, and TI sensors have more than one integrating circuit, indicating more robust signal processing.

2.2 Theory of Operation

While the sensors vary in signal processing, the optical components and geometry of the optical chamber are identical across all models. Fig. 1(b) shows the internal optical chamber of the sensors. An infrared emitting diode illuminates particles passing through the chamber. Light scattered by the particles at 60° is focused by a lens and collected on a photodiode, generating a current. The photocurrent is converted to a voltage in the transimpedance amplification stage. The voltage signal may then be amplified and filtered using band pass circuits. The design of the transimpedance and amplification stages varies from sensor-to-sensor.

2.3 Experimental Design

2.3.1 Particulate matter chamber

To characterize and compare the different sensors, one of each sensor model (six total) was placed in a controlled environment and exposed to smoke incense particles (Fig. 2). Incense

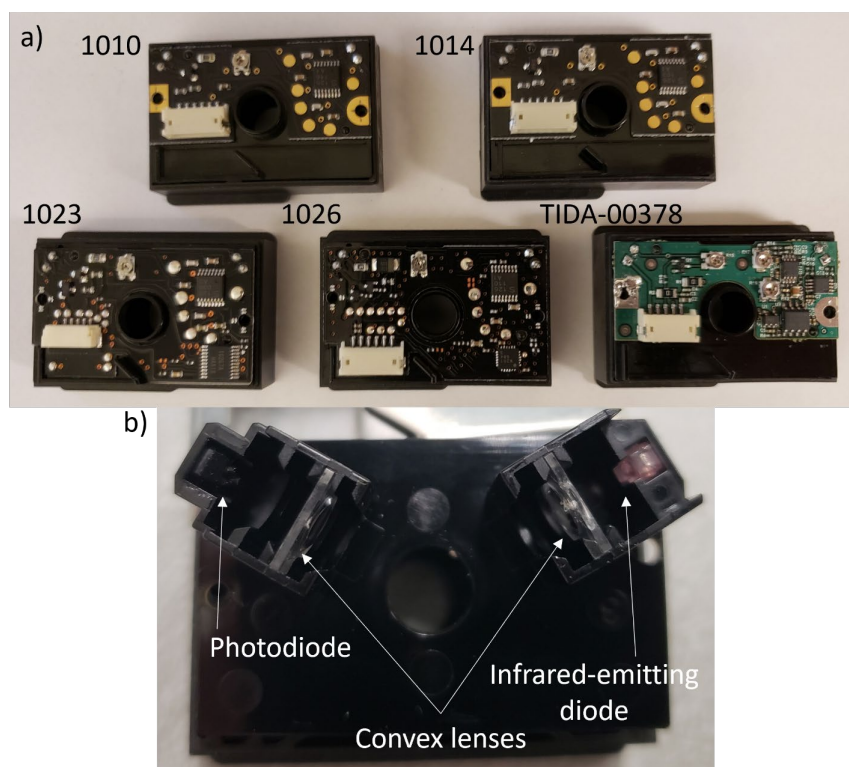
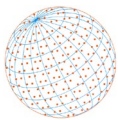


Fig. 1. Sensor internals. a) Printed circuit boards of each sensor for each model. Full model numbers beginning with “10” are preceded by “GP2Y” and followed by “AU0F”. b) Optical chamber of sensors, shared among all sensors.

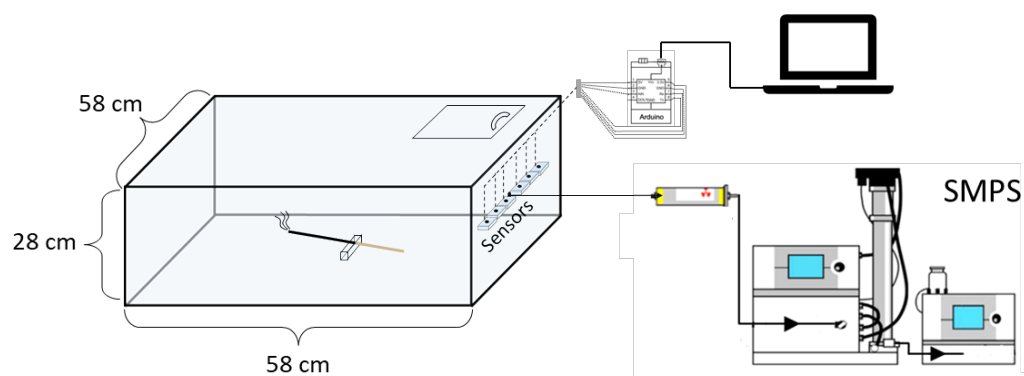
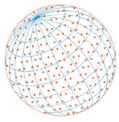


Fig. 2. Experimental setup. The plexiglass chamber is 0.1 m³ in volume.

particles have been used widely as a test aerosol due to their easy generation and similarity to indoor pollutant aerosols (Cheng *et al.*, 1995; Dacunto *et al.*, 2013; Wang *et al.*, 2015). Incense particles are also spherical (Chang *et al.*, 2007), meeting the criteria for Mie Theory as an adequate light scattering model. The newly-purchased sensors were mounted to the inside wall of a 0.1 m³ plexiglass chamber with the center hole facing downward. Communication and power wires were fed through feedthrough holes in the chamber, and gaps were snugly closed with rubber stoppers. Air was sampled from a port close to the sensors by a Scanning Mobility Particle Sizer (SMPS; TSI Inc., model 3938) consisting of an ⁸⁵Kr neutralizer (TSI Inc., model 3077A), a differential mobility analyzer (DMA; TSI Inc., model 3081), and a condensation particle counter (CPC; TSI Inc., model 3750). The DMA was operated at a sheath flow of 5 L min⁻¹ and aerosol flow of 1 L min⁻¹. For the first experiment, a burning incense stick was placed at the center of the chamber. The chamber filled with particles until exceeding all sensor outputs were saturated. The incense stick was then



removed, and data collection started. The chamber used was characterized in a previous study (Wang *et al.*, 2015) which determined the optimal conditions for ensuring an even PM distribution in the chamber. No forced convection was used in the chamber because it results in uneven spatial distributions of particles. Instead, particles were transported by random diffusion, resulting in a relatively even concentration in the chamber. Over the course of the experiment (approximately 2.5 hours), the PM concentration in the chamber exponentially decayed due to particle losses due to gravitational settling and diffusion to the walls. The sensor output was compared to the reference concentrations and size distributions provided by the SMPS to calculate sensor characteristics. Particles larger than the largest measured size by the SMPS (425 nm) were accounted for by fitting the particle size distribution to a lognormal distribution, then integrating across the fitted distribution from 10 nm to 2.5 mm to obtain the total mass concentration:

$$M_{tot} = \frac{\pi}{6} \rho_p \int_{d_p} n(d_p) d_p^3 d(d_p) \quad (1)$$

where $n(d_p)$ is the fitted lognormal particle size distribution function, and ρ_p is the smoke particle density (1.1 g cm^{-3}) (Ji *et al.*, 2010).

2.3.2 Sensor control routine and data collection

Power, control, and communication with the sensors was managed using an Arduino Uno microcontroller and performed per user manual instructions. Because the IRED will overheat if powered for long times, it was flashed at a duty cycle of 3.2% at 100 Hz frequency. The photodiode signal was sampled 280 μs after the IRED was engaged to allow full development of the signal, per the user manual. Manual powering of the IRED was not necessary for the 1023 and 1026, as these have built-in microcomputers that control the IRED. While the maximum sampling rate of the sensors is 100 Hz (except for 1026), the timescale of the chamber experiments is on the order of hours, so a less frequent sampling routine was used. Sensor output was sampled four times per second and averaged, logging one data point once per second. A one-by-one pairing of sensor data and SMPS reference data was performed offline by averaging across 60 sensor data points to match the sampling rate of the SMPS, which had a sampling frequency of once per minute. For the 1026 sensor, the output was logged at the maximum sampling rate of approximately 1 Hz. SMPS output was collected using Aerosol Instrument Manager (TSI, Inc.).

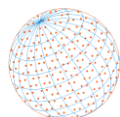
2.4 Performance Parameters

To systematically characterize and compare the sensors, performance parameters central to sensor performance were calculated based on the sensors' response to smoke particles in the particulate matter chamber. Sensitivities, precisions, accuracies, limits-of-detection, and saturation limits for each sensor were calculated. Fig. 3 shows an example sensor output plotted against a reference concentration and illustrates how performance parameters manifest themselves in the sensor's response to variable concentration.

Table 2 summarizes the performance parameters that were determined for each sensor, and the corresponding method to obtain them. Each performance parameter is described in detail in the following sections.

2.4.1 Sensitivity

A fundamental parameter of an ensemble light scattering sensor is its sensitivity to light, describing how much the sensor's response changes with an incremental increase in incident light onto the photodiode. A sensor's light sensitivity is a hardware-dependent constant that is inherent to the sensor (Li and Biswas, 2017), determined by the gain state of the photodiode amplification circuit. Sensitivity is often also described by the change in sensor response with an increase in PM mass concentration (Fig. 3(a)). While the mass-based description of sensitivity is useful for calibration purposes, it is not universal because its value will change based on the size distribution, shape, and composition of the aerosol (Li and Biswas, 2017). Hence, sensitivity will be presented with both definitions for generalizability. Light sensitivity depends on both the type



of photodiode and how the signal is processed, for example any gain and filter stages. Because sensors studied in this paper have the same optical components, we will be effectively comparing the signal processing hardware.

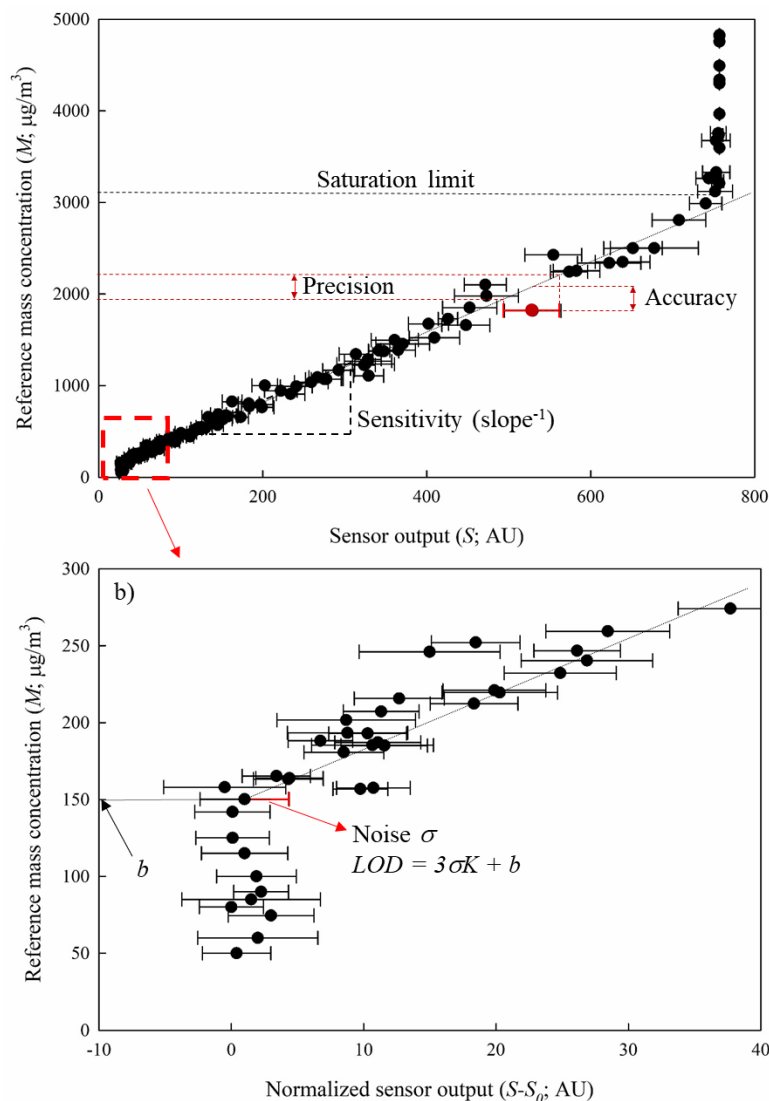
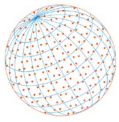


Fig. 3. Example light scattering sensor response to varying particulate matter concentration. Performance parameters shown in full concentration range a) sensitivity, saturation limit, precision. Low-concentration range b) noise, and limit of detection (LOD). Sensor output units shown as analog-digital conversion counts (arbitrary units).

Table 2. Experimental plan.

#	Performance parameter	Method
1	Sensitivity to light and mass concentration	Correlate sensor output with total scattered light and mass concentration during the chamber experiment.
2	Precision of measurements	Calculate absolute and relative standard deviations at each time interval in calibration curve.
3	Accuracy	Calculate average error across time intervals.
4	Limit of detection	Calculate standard deviation at blank conditions coupled with calibration curve parameters.
5	Saturation limit	Extrapolate calibration curve to known saturation value of sensor.



Sensitivity to light is experimentally determined in this study by correlating the sensor output (S) normalized by the baseline output (S_0) to the light scattered by incense particles (I) during the experiment. The baseline output is the output of the sensor in the absence of particles, arising from reflected infrared light inside the optical chamber (Bučar *et al.*, 2020). The size-dependent light scattered by each smoke particle in the sensing region during the experiment ($i(d_p)$) is approximated by applying Mie Theory coupled with the particle size distribution ($n_d(d_p)$) measured by the SMPS. The PyMieScatt python package (Sumlin *et al.*, 2018a) was used to obtain the Mie solution. A refractive index of $1.56 + 0.001i$ was assumed (Sumlin *et al.*, 2018b).

$$I = \int i(d_p) n_d(d_p) d(d_p) \quad (2)$$

A linear regression was performed to obtain the light sensitivity ($1 K_l^{-1}$) [Sensor output \times m² W⁻¹].

$$I = K_l (S - S_0) + b_1 \quad (3)$$

Sensitivity to mass concentration is determined by integrating the number distribution provided by the SMPS to a total mass concentration (Eq. (1)), by assuming spherical particle shape and a smoke particle density of 1.1 g cm^{-3} (Ji *et al.*, 2010). The integral was evaluated from 10 nm to 2.5 μm to represent PM_{2.5}. A linear regression was performed to obtain the mass sensitivity ($1 K_m^{-1}$) [Sensor output \times m³ μg^{-1}] (Fig. 3(a)).

$$M = K_m (S - S_0) + b_2 \quad (4)$$

The y-intercepts of the calibration curves, b_1 and b_2 , are inputs into determining the limit-of-detection (Section 2.4.4). These parameters physically represent the smallest concentration that can be measured over long periods of constant concentration.

2.4.2 Precision of measurement

Precision of measurement describes the repeatability of a measurement under constant conditions. High precision is desirable when small differences in concentration must be detected. It is quantitatively described by the standard deviation of sensor response during a period of constant conditions (Petrozzi, 2012), in this case constant particulate matter concentration in the optical chamber. The standard deviation can be expressed on an absolute scale, in units of concentration ($\sigma_i \times K_m$), or relative scale, in terms of percentage of the raw signal ($\sigma_i / (S_i - S_0)$) (Wang *et al.*, 2015). The absolute standard deviation is useful for understanding the extent to which the actual measurement is expected to fluctuate, while the relative standard deviation helps identify if differences in precision between sensors stem from sensitivity differences or noise level differences. Both relative and absolute standard deviations were calculated as a function of reference mass concentration.

Assuming a perfectly constant concentration between individual outputs, signal noise determines the precision level. Signal noise in light scattering sensors stems from the mechanism of photocurrent generation in the photodiode, as well as within the signal processing. In the photodiode, noise sources include shot noise, thermal noise, and dark current noise (Hui, 2019). Shot noise arises from statistical fluctuations in photons striking the photodiode surface. Thermal noise arises from electron-hole pairs generated from thermal motion of charge carriers. Dark current arises from the structure and composition of the photodiode. Noise is also generated through external electromagnetic interference and from amplification stages (Martinez and Stout, 2015; Sharp, 2020). Noise can be mitigated by applying a reverse or zero-volt bias on the photodiode, preventing leakage current that results in noise (Orozco, 2013; Martinez and Stout, 2015). Signal filter circuits also reduce noise and are implemented differently in the sensors evaluated in this study.

For each sampling interval, sensor readings were averaged, and the standard deviation was calculated. The standard deviation was then multiplied by the calibration parameter K_m , calculated from linear regressions (Section 2.4.1), to convert to a concentration value (Fig. 3(a)). This converted



value, in units of mass concentration, is reported as a function of reference mass concentration during that sampling interval.

2.4.3 Accuracy

A low-cost light scattering PM sensor outputs an analog value that requires a calibration curve to convert it to a concentration value. Typically, calibrations involve performing a linear regression to relate the raw sensor output to a referenced concentration. The error between predicted values based on the sensor's individual output coupled with the calibration curve, and the referenced value (M_{ref}), determines the sensor's accuracy (Petrozzi, 2012). Hence, sensors exhibiting strong linearity with reference measurements are more accurate.

To quantify accuracy, the error of each calibrated sensor output to each reference value was calculated and averaged across the dataset.

$$Error = |[K_m(S - S_0) + b_2] - M_{ref}| \quad (5)$$

2.4.4 Limit of detection

The limit of detection (LOD) describes the lowest concentration beyond which the sensor measures an above-baseline value (Fig. 3(b)) (Kaiser and Specker, 1956; Long and Winefordner, 1983; Wang *et al.*, 2015). A single sensor output below the LOD cannot be confidently distinguished from sensor noise. This parameter is crucial for selecting the appropriate sensor for the low-concentration applications; A lower LOD is desired for measurement of low concentrations that may be sub-LOD for many sensors. For example, a sensor aimed at measuring air quality for determining safe breathing conditions must have an LOD below around $15 \mu\text{g m}^{-3}$, the current World Health Organization 24 hour average $\text{PM}_{2.5}$ concentration limit (WHO, 2021). The LOD is quantified here as the calibrated mass concentration output three standard deviations (s) above the baseline value (Kaiser and Specker, 1956). The standard deviation is calculated from five minutes of sensor output (300 data points) after the chamber is filled with particle-free air.

$$LOD = 3\sigma K_m + b_2 \quad (6)$$

2.4.5 Saturation limit

The saturation limit is the maximum concentration value or light intensity the sensor can accurately measure (Austin *et al.*, 2015), beyond which the output plateaus out (i.e., is "maxed-out" or "saturated"), as seen in the vertical line in Fig. 3(a). This characteristic is determined by both photodiode-dependent properties and the gain of the photodiode current in signal processing (Thorlabs, 2023). For sensor applications relating to high PM environments, such as industrial settings or dust storms, a sensor with a high saturation value is needed to properly monitor dust concentrations.

The saturation limit can be determined experimentally by observing the concentration at which the sensor's value begins to drop from saturation during the smoke chamber experiment. It can also be calculated based on the calibration curve parameters and the known saturation value from the sensor (S_{max}). The latter method was used because, during early phases of the experiment where concentrations were near saturation limits, the concentration in the chamber was changing too fast for the one-minute sampling interval to accurately estimate the saturation limit.

$$Saturation\ limit = K_m (S_{max} - S_0) + b_2 \quad (7)$$

3 RESULTS AND DISCUSSION

3.1 Calibration Curves

Fig. 4 shows the normalized output of the sensors (baseline subtracted) plotted against the reference mass concentration calculated from the SMPS particle size distribution. All sensors

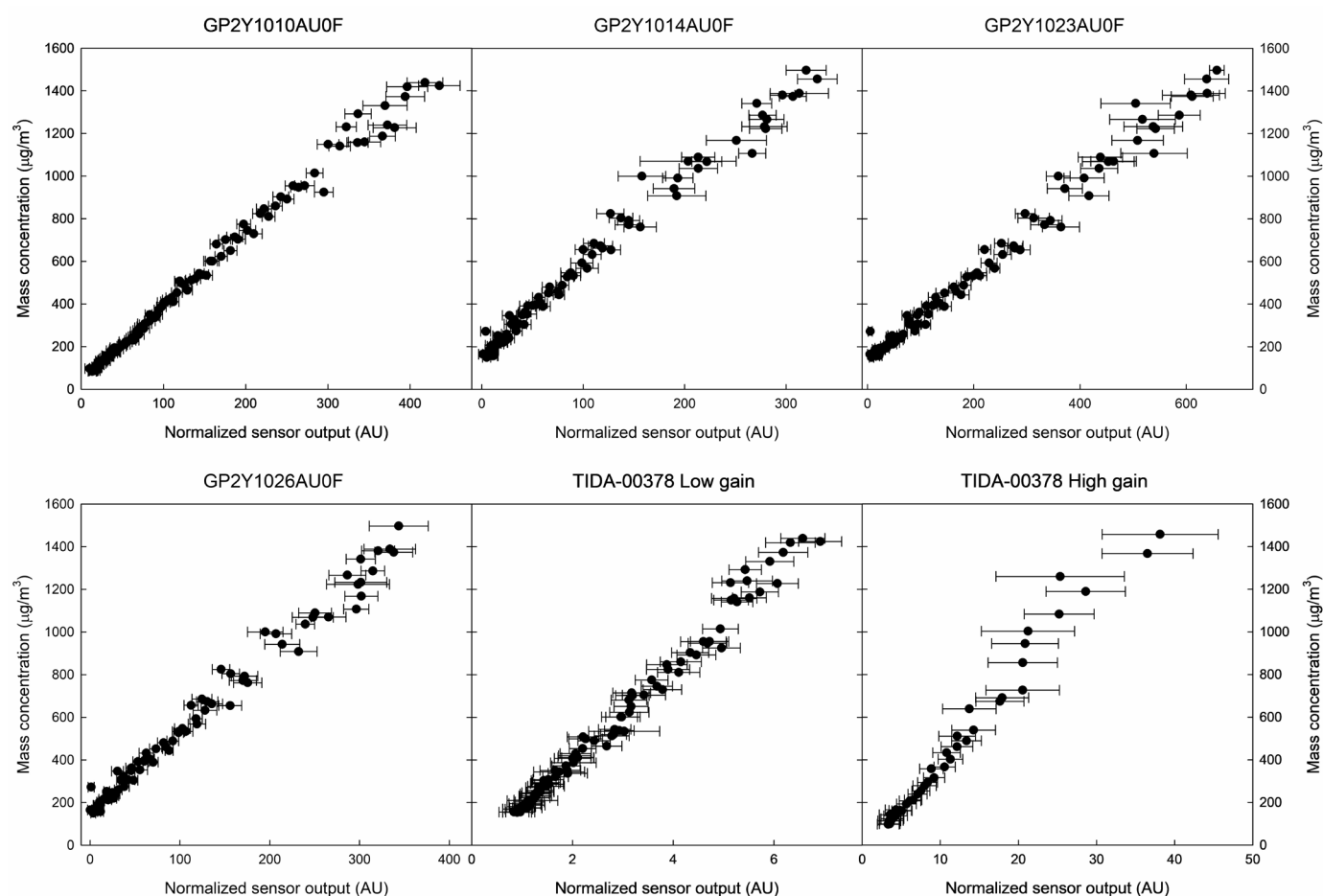


Fig. 4. Correlations between each sensor's output and the reference mass concentration calculated from SMPS measured particle size distribution. Error bars represent one standard deviation across 60 analog signals. Sensor output units shown as analog-digital conversion counts (arbitrary units).

exhibited excellent linearity against the reference, some to a greater extent than others. All R^2 values (Table 3) exceeded 97%, with the 1010 sensor showing the strongest linearity and the high-gain TI sensor showing the lowest linearity. The strong linearity of the Sharp sensors is consistent with previous calibrations performed on the Sharp GP2Y1010 (base model) sensor (Wang *et al.*, 2015; Sousan *et al.*, 2016; Li and Biswas, 2017), all of which reported R^2 values > 0.97 . The x-axis scale changes from sensor to sensor, indicating different sensitivity levels. In particular, the Texas Instruments sensors exhibited very low sensitivity, as indicated by the low output values on the x-axis; sensitivities this low have not been reported in previous studies to the author's knowledge. The size of error bars corresponds to the precision of measurement. Data points are more densely distributed at lower concentrations because of the exponential decay of concentration in the chamber; High concentration data points are fewer because of the rapidly-decaying concentration in the chamber. Reference mass concentrations during the experiment ranged from approximately 100 to $4 \times 10^4 \mu\text{g m}^{-3}$, however high concentrations were very unstable, decaying significantly during the one-minute sampling interval. Therefore, data presented and used for calibration curves are after $< 100 \mu\text{g m}^{-3}$ change was observed between the one-minute SMPS scans; at the high concentration end of the datasets presented, the drop in concentration in one minute was close to $100 \mu\text{g m}^{-3}$, whereas at lower concentrations, the drop in concentration was approximately $10 \mu\text{g m}^{-3}$. This criterion was met for concentration values below $1500 \mu\text{g m}^{-3}$. Previous calibration efforts on the Sharp base model (Wang *et al.*, 2015; Li and Biswas, 2017) similarly report more data points at lower concentrations as the same calibration procedure was used. While temporal variations in concentration within the sampling interval still occurred below



Table 3. Sensitivity parameters for light detection and particulate mass detection of incense smoke particles. GP2Y1023AU0F exhibits the highest sensitivity, while the low-gain TIDA-00378 exhibits the lowest sensitivity.

Sensor Model	Light sensitivity ($\text{m}^2 \text{W}^{-1} \times 10^9$)	Mass sensitivity ($\text{m}^3 \mu\text{g}^{-1}$)	R^2
GP2Y1010AU0F	1.86	0.296	0.993
GP2Y1014AU0F	1.56	0.247	0.986
GP2Y1023AU0F	3.16	0.492	0.987
GP2Y1026AU0F	1.68	0.267	0.985
TIDA-00378, low gain	0.028	0.004	0.988
TIDA-00378, high gain	0.1085	0.024	0.974

this cutoff, introducing error into the presented accuracy and precision parameters at the higher, rapidly-changing concentrations, one can still draw comparisons between sensors. Additionally, on the lower end of concentration towards the end of the experiment, data points were excluded beyond the baseline concentration to improve linearity. An uncropped version of these calibration curves would appear as is shown in Fig. 3. The linearity of the calibration curves also indicates that assumption of spherical particle shape was adequate. Incense particles, while initially spherical (Chang *et al.*, 2007), may have aggregated via Brownian coagulation during the experiment. This phenomenon was observed in a previous study on incense particles (Chuang *et al.*, 2011). Size distributions measured during the experiment (Fig. S2) shifted slightly towards larger particles, further suggesting aggregation of particles. However, significant changes in the particle size distribution would affect the slope of calibration curves (K_m in Eq. (4)). Because strong linearity was observed across all sensors, changes in particle size distribution shape were negligible, and further, the use of electrical mobility diameter to approximate particle size and mass was adequate. However, the reference mass concentrations, based on electrical mobility diameter, may be subject to error due to the spherical assumption, resulting in error in the magnitude of the calculated performance parameters. The true mass concentration of the aerosol is likely lower than that measured by the SMPS because aggregated, “fluffy”, smoke particles experience comparable drag forces as solid spheres with larger volumes (Chakrabarty *et al.*, 2007). Per Eqs. (3), (4), and (6), overestimating the reference mass concentration would result in *overpredicted* sensitivity, absolute precision, LOD, and saturation limit. The absolute magnitude of these parameters may be sought out by using a reference instrument that directly measures mass concentration such as a real-time filter-based approach (e.g., TEOM), or by utilizing an aggregate mobility analysis correction tool. Comparisons between sensors, however, can be made through estimations of mass concentration.

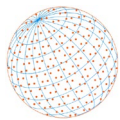
3.2 Performance Parameters

3.2.1 Sensitivity

Slopes in Fig. 4 are inversely proportional to mass sensitivity. Light sensitivity was determined by constructing a similar plot with the total scattered light on the y-axis (calculated using Eq. (2)) and performing a linear regression. Both sensitivity parameters are presented because mass sensitivity gives a general sense of suitability for the application but will vary based on the size distribution and composition of the aerosol used. In contrast, light sensitivity is a characteristic value of the sensor because the sensor is directly measuring optical power. Light sensitivity can be converted to an aerosol-dependent mass sensitivity if the size distribution, size-dependent light scattering characteristics, and particle density are known (Li and Biswas, 2017). By rearranging Eqs. (3) and (4), the mass sensitivity can be described in terms of light sensitivity.

$$K_m = \frac{K_l (M + b_2)}{I + b_1} \quad (8)$$

where M and I are the total mass and scattered light by the aerosol, integral properties of the



particle size distribution that can be calculated with sufficient knowledge or approximations of the aerosol to be measured (Li and Biswas, 2017). b_2 can be calculated by first determining the aerosol number concentration corresponding to the intercept b_1 (Eq. (3)), then integrating across the size distribution at that number concentration (Eq. (1)).

Mass and light sensitivity values are presented in Table 3. The ranked order of sensitivity is the same between light and mass sensitivity. This is expected because total scattered light and mass concentration are directly proportional for an aerosol of consistent size distribution. The sensitivities of Sharp-made sensors are on the same order of magnitude. The 1023 exhibits the highest sensitivity, exceeding the 2nd most sensitive sensor by approximately 66%. The 1014 is the least sensitive, but by a much smaller margin of 7%. The high sensitivity of the 1023 is consistent with the manufacturer claim (Sharp, 2023). The TI sensors of various gain states exhibited sensitivities more than an order of magnitude below that of the Sharp sensors. The low-gain TI sensor exhibits the lowest sensitivity, approximately one order of magnitude below the high gain TI sensor and two orders below the Sharp sensors. Despite the highest-gain potentiometer settings, the high-gain TI sensor still ranked the 2nd least sensitive sensor. Hence, if even higher sensitivity is desired, either an off-the-shelf Sharp model must be used, or new components must be selected on the TI circuit board to enable higher gain.

A mass sensitivity of $0.196 \text{ m}^3 \mu\text{g}^{-1}$ was reported in a previous study (Wang *et al.*, 2015) for a Sharp GP2Y sensor measuring incense particles, approximately 33% lower than the sensitivity measured in the present study. The difference may be explained by a variety of factors. Sensitivity variations are expected between sensors of the same model due to slight variations in electronic components and assembly processes. Additionally, the reference used by Wang *et al.* (2015) was an optical monitor that measured $\text{PM}_{2.5}$ whereas the present study used an SMPS with extrapolated mass concentration, allowing us to consider particles larger than 2.5 microns. Hence, reference monitors with a detectable size range that well-encompasses the calibration aerosol (e.g., Aerodynamic Particle Sizer (Sousan *et al.*, 2016)) must be utilized to accurately determine sensor performance parameters.

3.2.2 Precision

The precision of each sensor, represented by the absolute standard deviation ($\sigma_i \times K_m$) and relative standard deviation ($\sigma_i/(S_i - S_0)$) at each point in the experiment is shown in Fig. 5. Across all sensors, precision by absolute standard deviation improves as concentration decreases, while precision by relative standard deviation improves at higher concentrations. This is consistent with other measurements of precision for similar PM light scattering sensors (Wang *et al.*, 2015). These shared trends can be attributed to experimental aspects. In an ideal experiment, a constant concentration would be present in the optical chamber during each sampling interval, so the extent of fluctuations in this period would solely represent precision. However, despite filtering out data by setting a cutoff in concentration change between sampling intervals, incremental changes in concentration during each one-minute sampling interval are unavoidable. Therefore, sensor outputs in the beginning of each sampling interval were slightly higher than at the end, to a greater extent at higher concentrations. This explains the upward nonlinearities in absolute precision at high concentrations (Fig. 5(a)). Statistical fluctuations in concentration in the sensors' sensing regions are also expected, which would cause fluctuations in sensor response. Because these temporal fluctuations were present to the same extent for all sensors, precision of measurement across the full concentration range presented can still be compared. Further, while precision values at high concentrations are meant only for sensor comparisons, those at lower concentrations can be treated as approximate absolute precision due to the consistent concentration in the optical chamber.

Because all sensors examined have the same photodiode, IRED, and optical chamber, differences in precision can be attributed to differences in signal handling. Differences in absolute precision (Fig. 5(a)) can be attributed to differences in both sensitivity and noise level, while differences in relative precision (Fig. 5(b)) only consider noise level. On an absolute scale (Fig. 5(a)), for low concentrations, the 1026 and 1023 sensors were the most precise, while for high concentrations, the 1010 and 1014 were the most precise, varying from 20 to $90 \mu\text{g m}^{-3}$, consistent with previous precision measurements (Wang *et al.*, 2015). The manufacturer reported that all GP2Y models

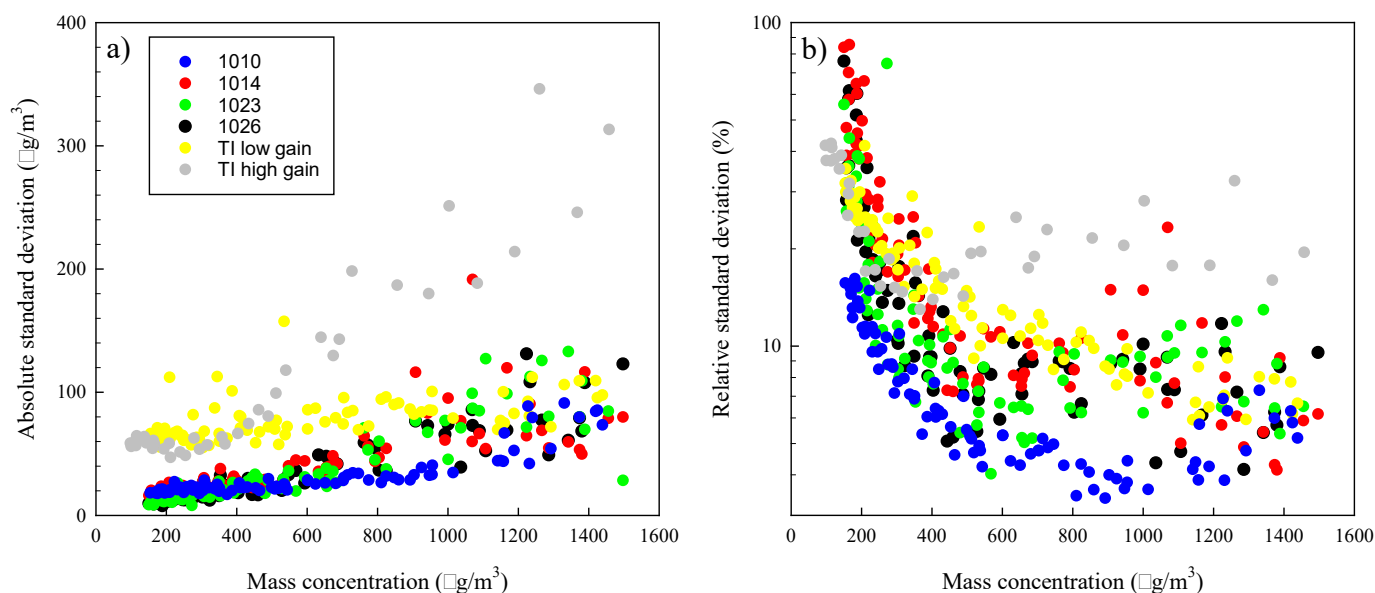


Fig. 5. Precision levels across different sensor models as a function of reference mass concentration. a) Absolute standard deviation, converted by calibration curve parameters. b) Relative standard deviation. Standard deviation calculated across 60 data points collected during sample interval.

besides the 1010 have a precision of $\pm 15\%$ (Sharp, 2023), and the 1010 has a precision of $\pm 30\%$ (Sharp, 2020), providing no information on how precision varies with concentration. The precision results collected here report the opposite; the 1010 is the only one of the GP2Y sensors that consistently exhibited a relative precision level below 15%, while others reached much higher relative standard deviation values at low concentrations. Measured precision may be improved had more data points were collected at each reference concentration. However, even if the manufacturer's experimental protocol for determining precision involved a larger number of data points (longer sampling interval), it is highly unlikely that the trend would be reversed.

The high-gain TI sensor had the poorest precision across most of the concentration range, attributed to its high noise level (Fig. 5(b)). Heightened noise may be the result of amplification of photodiode noise to a greater extent than other sensors. In contrast, the low precision of the low-gain TI sensor appeared to be a result of its low sensitivity, as seen by its high values in Fig. 5(a) but comparable values in Fig. 5(b). The relative precision of the low-gain TI sensor improved with increasing concentration more rapidly than other sensors such as the 1010, potentially making it the most precise at higher concentrations than measured in the experiment. The absolute standard deviation curve was also the flattest, indicating less of a dependency on concentration. This may be the case because the low-gain sensor is only operating in a small fraction of its measurement range at the concentrations shown in Fig. 5.

3.2.3 Accuracy

Sensor accuracy, described by the average error between the calibrated output of the sensor and the reference concentration (Eq. (5)), is shown in the second column of Table 4. The 1010 model was the most accurate of all the sensors despite being the base model. This arises from its strong linearity (Table 3). Wang *et al.* (2015) similarly reported the GP2Y1010 as the most accurate low-cost sensor when compared to two other nephelometers. An accuracy value, in terms of mass concentration, was however not reported. The least accurate sensor was the low-gain TI sensor, which exhibited the poorest linearity. Other sensors exhibited accuracies that were similar to the 1010, with the low-gain TI sensor ranking 2nd most accurate. However, our results do not cover how accuracy varies between sensors of the same model. Hence, future work should examine this aspect in order to definitively determine which sensors are the most accurate on a broader level. As in the case of precision, accuracy can also be described as a function of



Table 4. Limits of detection, saturation limits, and accuracies for different sensor models. Limits of detection were calculated using the standard deviation at sensor baseline and calibration parameters. Saturation limits were calculated using the calibration parameters and the known analog saturation value of the sensors. Accuracy is the error between converted sensor output and reference mass concentration averaged across the experiment.

Sensor Model	Accuracy ($\mu\text{g m}^{-3}$)	LOD ($\mu\text{g m}^{-3}$)	Saturation limit ($\mu\text{g m}^{-3}$)
GP2Y1010AU0F	25.7	79.1	2200
GP2Y1014AU0F	34.0	205	2840
GP2Y1023AU0F	30.3	148	1540
GP2Y1026AU0F	36.0	186	2900
TIDA-00378, low gain	30.2	370	152000
TIDA-00378, high gain	50.9	273	28460

concentration, and both in absolute and relative units. Accuracy as a function of concentration is shown in the Supporting information (Fig. S1). Because there was only a weak dependency, error was averaged across all concentrations as an overall representation of accuracy.

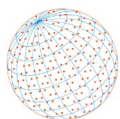
Reported accuracies of low-cost sensors in field studies ($R^2 = 0.27\text{--}0.87$ (Tagle *et al.*, 2020), 0.53 (Gao *et al.*, 2015), 0.4–0.95 (Gramsch *et al.*, 2021), 0.86 (Ghamari *et al.*, 2022)) are notably lower than those of the present study and previous laboratory calibration efforts (Wang *et al.*, 2015; Sousan *et al.*, 2016; Li and Biswas, 2017). A field study with the Sharp GP2Y1010 (Ghamari *et al.*, 2022) found that the Sharp sensor exhibited higher accuracy in the lab than in the field, explained by rapid changes in concentration. When monitoring concentrations in the field, spatial variations in concentrations may occur based on the physical location of the sensor relative to the reference monitor. This would result in significant differences between calibrated sensor output and reference concentration that are not attributed to error. A smoothing algorithm applied to the sensor output, such as a moving average, may overcome such issues. The glaring drawback of low-cost photometers is aerosol-dependent calibration; this is a significant source of error, making optical particle counters (He *et al.*, 2020) advantageous if aerosols of unknown characteristics are to be measured in the field.

3.2.4 Limit of detection

LODs calculated with Eq. (6) are shown in the third column of Table 4. The LOD depends on a combination of parameters presented: sensitivity, baseline value, and precision. The 1010 exhibits the lowest LOD while the low gain TI is the highest by approximately $300 \mu\text{g m}^{-3}$. The LOD of the low-gain TI is very high because of its low sensitivity; Three standard deviations above the baseline value translates to a very high increase in concentration because of the low sensitivity. The manufacturer does not report LODs for the various models. A “reference detection concentration” is provided, with what appears to be a range of concentrations, all of which start with $0 \mu\text{g m}^{-3}$ (Sharp, 2023). This is a misleading claim, as the calculated LODs show that no sensor in the Sharp lineup can measure dust from a single measurement below a concentration of approximately $80 \mu\text{g m}^{-3}$.

Note that the LOD values in Table 4 appear to be within the linear portions of calibration curves in Fig. 4. For example, the LOD for the low-gain TI sensor $370 \mu\text{g m}^{-3}$, but there is clear linearity for concentrations below this level. This is because the LOD refers to the lowest concentration, calculated from an *individual sensor output*, that significantly deviates from baseline. Data points in the calibration curves below the LOD still exhibit linearity because there are enough data points during the sampling interval for the average value to fall onto the calibration curve. Hence, concentrations below the LOD can be measured, given that sufficient data points are collected and averaged, and the concentration of the environment is not rapidly changing. In such an environment, the minimum detection level is instead determined by the y-intercept of the calibration curve (i.e., b_2 in Eq. (4)).

Both LODs (Table 4) and intercept values from Fig. 4 are high (LODs $> 70 \mu\text{g m}^{-3}$; $b_2 > 50 \mu\text{g m}^{-3}$), relative to $\text{PM}_{2.5}$ standards for breathable air (EPA: $12 \mu\text{g m}^{-3}$; WHO: $5 \mu\text{g m}^{-3}$). This suggests the GP2Y sensors may be more suitable for monitoring high concentration environments such as dust



storms or wildfire events. The sensors may be suitable for monitoring lower concentrations if different aerosols are measured; an aerosol containing larger and non-absorbing particles would exhibit a lower limit-of-detection than the small, absorbing smoke aerosol used in this study.

The LOD reported for two Sharp GP2Y1010 sensors in a previous study (Wang *et al.*, 2015) was 26.1 and 26.9 $\mu\text{g m}^{-3}$, notably lower than our reported 79.1 $\mu\text{g m}^{-3}$. The presently reported LOD is higher because a different quantification of LOD was used. The IUPAC LOD definition (Long and Winefordner, 1983) was used, which considers the intercept value in the calibration curve (i.e., b_2 in Eq. (4)), whereas Wang *et al.* (2015) assumed that the calibration curve intercepts the origin (i.e., LOD is only dependent on noise). If we had used the LOD formulation from Wang *et al.* (2015), our 1010 LOD value would be 31.5 $\mu\text{g m}^{-3}$. This LOD value is not realistic because it falls below the y-intercept of the calibration curve. Further, their also appears to fall below the y-intercept of their reported calibration curve. Hence, future studies should use the LOD formulation factoring in the y-intercept of the calibration curve.

3.2.5 Saturation limit

The calculated saturation limits for each sensor (Eq. (7)) are shown in the fourth column of Table 4. Because the sensors had approximately the same saturation value (~ 700 ADC units), the saturation value was determined by sensitivity. The 1023 had the lowest saturation limit of 1540 $\mu\text{g m}^{-3}$. Within the off-the-shelf Sharp sensors, the 1026 had the highest saturation value. This finding is consistent with the reported feature of the 1026 of “high concentration”. The low-gain TI sensor had the highest saturation limit of 152,000 $\mu\text{g m}^{-3}$ (152 mg m^{-3}). The low gain TI sensor was the only sensor to not reach saturation limit during the experiment. The high gain TI sensor also had higher saturation limit than that of the Sharp sensors, consistent with the sensitivity trends.

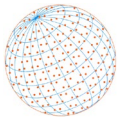
Saturation limits for the Sharp sensors have not been directly reported in previous studies. However, the Sharp GP2Y1010 calibration curve from Wang *et al.* (2015) for sucrose particles reveal a very low saturation value of approximately 150 $\mu\text{g m}^{-3}$, notably lower than our reported 2200 $\mu\text{g m}^{-3}$. The aerosol composition and size distribution affects the saturation value; aerosols containing larger and more scattering particles will saturate the sensor at lower concentrations than aerosols with smaller, absorbing particles like the incense particles used in the present study.

3.3 Importance of Performance Parameters on Sensor Selection

The appropriate particulate matter sensor should be selected depending on several constraints including the environment of application, desired output measurements, degree of spatiotemporal resolution, and price. Light scattering sensors are useful when concentration is the desired output and fine spatiotemporal resolution is needed, enabled by their low cost. If particle size information is needed, an optical particle counter is more suitable for the job. The LOD and saturation limit performance parameters indicate if the sensor is an appropriate choice for the anticipated concentration range of the intended application environment. The low-gain TI is an appropriate choice for environments with very high particulate mass concentrations. However, the low-gain TI also has the highest LOD, indicating a tradeoff between LOD and saturation limit. If an upper concentration limit less than a few mg m^{-3} is anticipated, the 1026 or 1014 would be suitable choices. The 1010 is also a reliable choice if concentrations do not surpass approximately 2 mg m^{-3} , because it demonstrated the highest accuracy and precision across a wide range of concentrations, along with mid-range sensitivity. The 1023 is a suitable choice if high precision is desired.

The difference in performance between the two TI sensors indicates that critical performance parameters discussed here can be selected by adjusting resistance values in the amplification stages. Future work may examine the effect of adjusting capacitance values in the signal filter stages to gauge the effect on noise (precision of measurements). The modularity of the TIDA-00378 sensors makes them potential assets for future sensor campaigns. Incorporation of digital potentiometers could enable remote or automated adjustment of the gain state based on monitoring of the output. For example, if sensor saturation occurs, the digital potentiometers could automatically adjust the resistance in the gain stage to minimize gain and collect valuable, sub-saturation data.

A limitation of the study is that only one of each sensor model was evaluated, hence the performance parameters calculated and presented in Tables 3 and 4 have associated uncertainty



values arising from product-to-product variability. A previous study (Wang *et al.*, 2015) examined intra-sensor variability of the Sharp GP2Y1010 model and found higher variability between sensors at higher concentrations. Future work should repeat the procedures outlined in this study with multiple of the newer Sharp sensors models to elucidate these variabilities. While it is likely the manufacturer has performed such testing as part of a quality control process, the data are not known by the author to be publicly available.

4 CONCLUSIONS

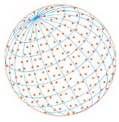
Six low-cost particulate matter sensors were systematically tested in a controlled particulate matter chamber in order to determine performance parameters intrinsic to the sensors. All sensors operated on the same optical components and geometry, isolating our analysis to the differences between sensors' signal processing circuitry. Four of the six sensors studied were models from the off-the-shelf Sharp GP2Y series (GP2Y 1010, 1014, 1023, and 1026 AU0F). The other two sensors were fabricated according to the analog frontend design from Texas Instruments (TIDA-00378); Potentiometers on one sensor were set to minimum gain and the other was set to maximum gain. The Sharp series sensors exhibited significantly higher sensitivity than the TI sensors, and measured sensitivities for the Sharp models were consistent with manufacturer claims. Precision of measurements showed a dependency on reference concentration, and the 1010 sensor showed the highest precision in terms of relative standard deviation. The low-gain TI sensor exhibited the highest LOD and saturation value, while the 1010 had the lowest LOD and the 1023 had the lowest saturation limit. This study provided a descriptive set of performance parameters for different models of the popular Sharp GP2Y dust sensors as well as the tunable TI sensor. More generally, we also demonstrated an experimental protocol for obtaining these characteristic performance parameters, crucial for guiding selection of the light scattering sensor that is well-suited for the PM measurement environment.

SUPPLEMENTARY MATERIAL

Supplementary material for this article can be found in the online version at <https://doi.org/10.4209/aaqr.230129>

REFERENCES

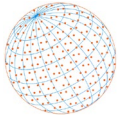
- Austin, E., Novosselov, I., Seto, E., Yost, M.G. (2015). Laboratory evaluation of the Shinyei PPD42NS low-cost particulate matter sensor. *PLoS One* 10, e0137789. <https://doi.org/10.1371/journal.pone.0137789>
- Baqer, N.S., Mohammed, H.A., Albahri, A. (2022). Development of a real-time monitoring and detection indoor air quality system for intensive care unit and emergency department. *Signa Vitae* 1, 16
- Baqer, N.S., Mohammed, H.A., Albahri, A.S. (2023). Development of a real-time monitoring and detection indoor air quality system for intensive care unit and emergency department. *Signa Vitae* 19, 77–92. <https://doi.org/10.22514/sv.2022.013>
- Bučar, K., Malet, J., Stabile, L., Pražnikar, J., Seeger, S., Žitnik, M. (2020). Statistics of a sharp GP2Y low-cost aerosol PM sensor output signals. *Sensors* 20, 6707. <https://doi.org/10.3390/s202306707>
- Cao, J., Chow, J.C., Lee, F.S., Watson, J.G. (2013). Evolution of PM_{2.5} measurements and standards in the US and future perspectives for China. *Aerosol Air Qual. Res.* 13, 1197–1211. <https://doi.org/10.4209/aaqr.2012.11.0302>
- Chakrabarty, R.K., Moosmüller, H., Arnott, W.P., Garro, M.A., Slowik, J.G., Cross, E.S., Han, J.H., Davidovits, P., Onasch, T.B., Worsnop, D.R. (2007). Light scattering and absorption by fractal-like carbonaceous chain aggregates: Comparison of theories and experiment. *Appl. Opt.* 46, 6990–7006. <https://doi.org/10.1364/AO.46.006990>



- Chang, Y.C., Lee, H.W., Tseng, H.H. (2007). The formation of incense smoke. *J. Aerosol Sci.* 38, 39–51. <https://doi.org/10.1016/j.jaerosci.2006.09.003>
- Cheng, Y., Bechtold, W., Yu, C., Hung, I.F. (1995). Incense smoke: characterization and dynamics in indoor environments. *Aerosol Sci. Technol.* 23, 271–281. <https://doi.org/10.1080/02786829508965312>
- Chuang, H.C., Jones, T., Chen, Y., Bell, J., Wenger, J., Bérubé, K. (2011). Characterisation of airborne particles and associated organic components produced from incense burning. *Anal. Bioanal. Chem.* 401, 3095–3102. <https://doi.org/10.1007/s00216-011-5209-7>
- Dacunto, P.J., Cheng, K.-C., Acevedo-Bolton, V., Jiang, R.T., Klepeis, N.E., Repace, J.L., Ott, W.R., Hildemann, L.M. (2013). Real-time particle monitor calibration factors and PM_{2.5} emission factors for multiple indoor sources. *Environ. Sci. Processes Impacts* 15, 1511–1519. <https://doi.org/10.1039/C3EM00209H>
- Drogramaci, M., Butt, M.A. (2021). The influence of slit lamp shield size and design in reducing aerosol transmission. *Transl. Vision Sci. Technol.* 10, 33–33. <https://doi.org/10.1167/tvst.10.13.33>
- Friedlander, S.K. (2000). *Smoke, Dust, and Haze*. Oxford university press New York.
- Gao, M., Cao, J., Seto, E. (2015). A distributed network of low-cost continuous reading sensors to measure spatiotemporal variations of PM_{2.5} in Xi'an, China. *Environ. Pollut.* 199, 56–65. <https://doi.org/10.1016/j.envpol.2015.01.013>
- Ghamari, M., Soltanpur, C., Rangel, P., Groves, W.A., Kecojevic, V. (2022). Laboratory and field evaluation of three low-cost particulate matter sensors. *IET Wireless Sens. Syst.* 12, 21–32. <https://doi.org/10.1049/wss2.12034>
- Ghizlane, F., Mabrouki, J., Ghrihi, F., Azrour, M. (2022). Proposal for a high-resolution particulate matter (PM₁₀ and PM_{2.5}) capture system, comparable with hybrid system-based internet of things: Case of quarries in the Western Rif, Morocco. *Pollution* 8, 169-180. <https://doi.org/10.22059/poll.2021.326846.1134>
- Gramsch, E., Oyola, P., Reyes, F., Vásquez, Y., Rubio, M., Soto, C., Pérez, P., Moreno, F., Gutiérrez, N. (2021). Influence of particle composition and size on the accuracy of low cost PM sensors: Findings from field campaigns. *Front. Environ. Sci.* 9, 751267. <https://doi.org/10.3389/fenvs.2021.751267>
- He, M., Kuerbanjiang, N., Dhaniyala, S. (2020). Performance characteristics of the low-cost Plantower PMS optical sensor. *Aerosol Sci. Technol.* 54, 232–241. <https://doi.org/10.1080/02786826.2019.1696015>
- Hui, R. (2019). *Introduction to fiber-optic communications*. Academic Press.
- Husar, R. (1974). *Recent developments in in situ size spectrum measurement of submicron aerosols*. ASTM International.
- Janssens-Maenhout, G., Crippa, M., Guizzardi, D., Dentener, F., Muntean, M., Pouliot, G., Keating, T., Zhang, Q., Kurokawa, J., Wankmüller, R. (2015). HTAP_v2. 2: a mosaic of regional and global emission grid maps for 2008 and 2010 to study hemispheric transport of air pollution. *Atmos. Chem. Phys.* 15, 11411–11432. <https://doi.org/10.5194/acp-15-11411-2015>
- Ji, X., Le Bihan, O., Ramalho, O., Mandin, C., D'Anna, B., Martinon, L., Nicolas, M., Bard, D., Pairon, J.C. (2010). Characterization of particles emitted by incense burning in an experimental house. *Indoor Air* 20, 147–158. <https://doi.org/10.1111/j.1600-0668.2009.00634.x>
- Kaiser, H., Specker, H. (1956). Bewertung und vergleich von analysenverfahren. *Fresenius' Zeitschrift für analytische Chemie* 149, 46–66.
- Kelleher, S., Quinn, C., Miller-Lionberg, D., Volckens, J. (2018). A low-cost particulate matter (PM_{2.5}) monitor for wildland fire smoke. *Atmos. Meas. Tech.* 11, 1087–1097. <https://doi.org/10.5194/amt-11-1087-2018>
- Khadem, M.I., Sgârciu, V. (2014). Smart sensor nodes for airborne particulate concentration detection. *U.P.B. Sci. Bull., Series C* 76, 3–12.
- Kumar, P., Morawska, L., Martani, C., Biskos, G., Neophytou, M., Di Sabatino, S., Bell, M., Norford, L., Britter, R. (2015). The rise of low-cost sensing for managing air pollution in cities. *Environ. Int.* 75, 199–205. <https://doi.org/10.1016/j.envint.2014.11.019>
- Lee, H., Kang, J., Kim, S., Im, Y., Yoo, S., Lee, D. (2020). Long-term evaluation and calibration of low-cost particulate matter (PM) sensor. *Sensors* 20, 3617. <https://doi.org/10.3390/s20133617>



- Li, J., Biswas, P. (2017). Optical characterization studies of a low-cost particle sensor. *Aerosol Air Qual. Res.* 17, 1691–1704. <https://doi.org/10.4209/aaqr.2017.02.0085>
- Li, J., Mattewal, S.K., Patel, S., Biswas, P. (2020). Evaluation of nine low-cost-sensor-based particulate matter monitors. *Aerosol Air Qual. Res.* 20, 254–270. <https://doi.org/10.4209/aaqr.2018.12.0485>
- Long, G.L., Winefordner, J.D. (1983). Limit of detection. A closer look at the IUPAC definition. *Anal. Chem.* 55, 712A–724A. <https://doi.org/10.1021/ac00258a001>
- Manikonda, A., Zíková, N., Hopke, P.K., Ferro, A.R. (2016). Laboratory assessment of low-cost PM monitors. *J. Aerosol Sci.* 102, 29–40. <https://doi.org/10.1016/j.jaerosci.2016.08.010>
- Martinez, G., Stout, D. (2015). *PM_{2.5}/PM₁₀ Particle Sensor Analog Front-End for Air Quality Monitoring Design*. Texas Instruments, pp. 1–44.
- Olivares, G., Longley, I., Coulson, G. (2012). Development of a low-cost device for observing indoor particle levels associated with source activities in the home. International Society of Exposure Science (ISES), Seattle, WA.
- Orozco, L. (2013). Programmable-gain transimpedance amplifiers maximize dynamic range in spectroscopy systems. *Analog Dialogue* 47, 1–5.
- Petrozzi, S. (2012). *Practical Instrumental Analysis: Methods, Quality Assurance, and Laboratory Management*. John Wiley & Sons.
- Pope, C.A., Burnett, R.T., Thun, M.J., Calle, E.E., Krewski, D., Ito, K., Thurston, G.D. (2002). Lung cancer, cardiopulmonary mortality, and long-term exposure to fine particulate air pollution. *JAMA* 287, 1132–1141. <https://doi.org/10.1001/jama.287.9.1132>
- Sharp (2015a). Data specification for dust sensor. Model no. GP2Y1023AU0F. http://www.socle-tech.com/doc/IC%20Channel%20Product/Sensors/Dust%20Sensor/GP2Y1023AU0F_spec_ED14G011A.pdf
- Sharp (2015b). Device specification for dust sensor. Model no. GP2Y1014AU0F. https://datasheet.lcsc.com/szlcsc/1905131608_Sharp-Microelectronics-GP2Y1014AU0F_C390729.pdf
- Sharp (2018). Specifications, dust sensor. GP2Y1026AU0F. https://datasheet.lcsc.com/lcsc/1912111437_Sharp-Microelectronics-GP2Y1026AU0F_C390730.pdf
- Sharp (2020). Compact Optical Dust Sensor. GP2Y1010AU0F https://global.sharp/products/device/lineup/data/pdf/datasheet/gp2y1010au_e.pdf
- Sharp (2023). Optical Electric Sensor Lineup. <http://global.sharp/products/device/lineup/selection/opto/dust/index.html>
- Sousan, S., Koehler, K., Thomas, G., Park, J.H., Hillman, M., Halterman, A., Peters, T.M. (2016). Inter-comparison of low-cost sensors for measuring the mass concentration of occupational aerosols. *Aerosol Sci. Technol.* 50, 462–473. <https://doi.org/10.1080/02786826.2016.1162901>
- Sumlin, B.J., Heinson, W.R., Chakrabarty, R.K. (2018a). Retrieving the aerosol complex refractive index using PyMieScatt: A Mie computational package with visualization capabilities. *J. Quant. Spectrosc. Ra.* 205, 127–134. <https://doi.org/10.1016/j.jqsrt.2017.10.012>
- Sumlin, B.J., Heinson, Y.W., Shetty, N., Pandey, A., Pattison, R.S., Baker, S., Hao, W.M., Chakrabarty, R.K. (2018b). UV–Vis–IR spectral complex refractive indices and optical properties of brown carbon aerosol from biomass burning. *J. Quant. Spectrosc. Radiat. Transfer* 206, 392–398. <https://doi.org/10.1016/j.jqsrt.2017.12.009>
- Tagle, M., Rojas, F., Reyes, F., Vásquez, Y., Hallgren, F., Lindén, J., Kolev, D., Watne, Å.K., Oyola, P. (2020). Field performance of a low-cost sensor in the monitoring of particulate matter in Santiago, Chile. *Environ. Monit. Assess.* 192, 171. <https://doi.org/10.1007/s10661-020-8118-4>
- Thorlabs (2023). Photodiode saturation and noise floor. [thorlabs.com. https://www.thorlabs.com/images/TabImages/Photodetector_Lab.pdf](https://www.thorlabs.com/images/TabImages/Photodetector_Lab.pdf)
- U.S. Environmental Protection Agency (U.S. EPA) (2022). List of Designated Reference and Equivalent Methods. Office of Research and Development, U.S. Environmental Protection Agency.
- Vidwans, A., Choudhary, S., Jolliff, B., Gillis-Davis, J., Biswas, P. (2022). Size and charge distribution characteristics of fine and ultrafine particles in simulated lunar dust: Relevance to lunar missions and exploration. *Planet. Space Sci.* 210, 105392. <https://doi.org/10.1016/j.pss.2021.105392>
- Wang, Y., Li, J., Jing, H., Zhang, Q., Jiang, J., Biswas, P. (2015). Laboratory evaluation and



- calibration of three low-cost particle sensors for particulate matter measurement. *Aerosol Sci. Technol.* 49, 1063–1077. <https://doi.org/10.1080/02786826.2015.1100710>
- White, R.M., Paprotny, I., Doering, F., Cascio, W.E., Solomon, P.A., Gundel, L.A. (2012). Sensors and ‘apps’ for community-based atmospheric monitoring. *EM Air Waste Manage. Assoc. Mag. Environ. Manage.* 5, 36–40.
- Williams, R., Kaufman, A., Hanley, T., Rice, J., Garvey, S. (2014). Evaluation of field-deployed low cost PM sensors. U.S. Environmental Protection Agency, Washington, DC. EPA/600/R-14/464 (NTIS PB 2015-102104).
- World Health Organization (WHO) (2021). WHO global air quality guidelines: particulate matter (PM_{2.5} and PM₁₀), ozone, nitrogen dioxide, sulfur dioxide and carbon monoxide. World Health Organization, Geneva.
- Zhou, M., Abdulghani, A.M., Imran, M.A., Abbasi, Q.H. (2020). Internet of Things (IoT) Enabled Smart Indoor Air Quality Monitoring System. Presented at the CNIOT2020: 2020 International Conference on Computing, Networks and Internet of Things, ACM, Sanya China, pp. 89–93. <https://doi.org/10.1145/3398329.3398342>